Geol. Mag. **143** (*2*), *2006, pp. 145–163. © 2006 Cambridge University Press*
doi:10.1017/S0016756805001482 *Printed in the United Kingdom*

Petrological evidence for crustal thickening and extension in the Serre granulite terrane (Calabria, southern Italy)

PASQUALE ACQUAFREDDA, ANNAMARIA FORNELLI*, ANTONIO PAGLIONICO & GIUSEPPE PICCARRETA

Dipartimento Geomineralogico, Bari University via E. Orabona, 4-70124 Bari, Italy

(*Received* 11 January 2005; *accepted* 22 August 2005)

Abstract – The paper presents the metamorphic trajectory recorded by metapelitic migmatites of the upper part of the Hercynian lower continental crust of the Serre (southern Calabria, Italy). The relict minerals, reaction textures and phase equilibria define a clockwise *P–T* path. The prograde metamorphism from temperature of about 500 °C and pressure of 4–5 kbar to $T < 700$ °C and $P \sim 8$ kbar stabilized the assemblage Grt + Ky + Bt + Ms(Si/11ox =3.26–3.29) in the uppermost metapelites of the profile. Progressive heating led to H_2O-fluxed and dehydration melting first of Ms, then of Bt at $T < 700$ °C in the stability field of sillimanite. This process was followed by nearly isothermal decompression producing additional melt with a transition from Grt to a Grt + Crd stability field. Further decompression caused the formation of Crd-corona around garnet. Nearly isobaric cooling led to rehydration and retrogression across the stability field of andalusite up to the stability field of kyanite. The lowermost metapelites of the studied profile have lost most of the memory of the prograde *P–T* path; they record decompression and cooling. High-temperature mylonites occur in which boudinage, elongation and pull-aparts characterize the porphyroclasts. The pull-aparts in the high-*T* mylonites are filled with low-*P* minerals (Crd + Spl). The Hercynian metamorphic trajectory and the microtextures are consistent with crustal thickening and subsequent extensional regime. During extension, an important tectonic denudation probably caused the isothermal decompression. Extension also occurred in post-Hercynian times as documented by pull-aparts in sillimanite porphyroclasts filled with chloritoid within a low-grade mylonite.

Keywords: Hercynian, migmatites, southern Calabria, P–T path.

1. Introduction

The reconstruction of *P–T* paths from metamorphic belts is essential for understanding orogenic processes and the tectonic settings of metamorphism (e.g. Brown, 1993). The recovery of information constraining the form of *P–T* paths, however, is not straightforward. The preservation of prograde segments of *P–T* paths is rare because the relics of the prograde path are eradicated as temperature and diffusion rates increase towards the metamorphic peak.

In the Serre, southern Calabria, a 7–8 km thick section of Hercynian lower crust (Schenk, 1984) crops out, which has been metamorphosed under granulite facies conditions. Kyanite has been described as both a relict phase within the uppermost metapelites (e.g. Paglionico & Piccarreta, 1978; Schenk, 1990) and, together with andalusite, as a retrograde mineral formed during cooling (Schenk, 1990). A Ky–Sil–And–Ky trajectory (mineral abbreviations according to Kretz, 1983) was proposed by Schenk (1990). It is characterized by strong heating and moderate pressure increase, followed by isothermal decompression and isobaric cooling. The geodynamic causes for decompression have been interpreted as reflecting either tectonic collision (Schenk, 1984, 1989, 1990; Graessner & Schenk, 2001) or extensional tectonics (Caggianelli, Prosser & Del Moro, 2000; Del Moro, Fornelli & Piccarreta, 2000*b*; Caggianelli & Prosser, 2002). In order to constrain the evolution of the lower crustal segment of the Serre we have revisited the upper part of the metapelitic migmatites (especially relict mineral parageneses). The occurrence of minerals and textures indicative of disequilibrium as well as the sequence of the partial melting reactions (Fornelli *et al*. 2002) in the metapelites of the upper part of the section gives us new information on the *P–T* trajectory. We show that the lower crustal segment of the Serre records metamorphic processes which can fit a model involving contractional and subsequent extensional regimes in pre-Alpine times.

2. Regional geological context

The Calabria–Peloritani Belt is an arcuate structure extending southward from the Apenninic chain of Italy (Fig. 1). It formed during Tertiary times as a consequence of the collision between Europe and Africa involving pre-Triassic terrains; whether these terrains belong to African or European continental

*Author for correspondence: a.fornelli@geomin.uniba.it

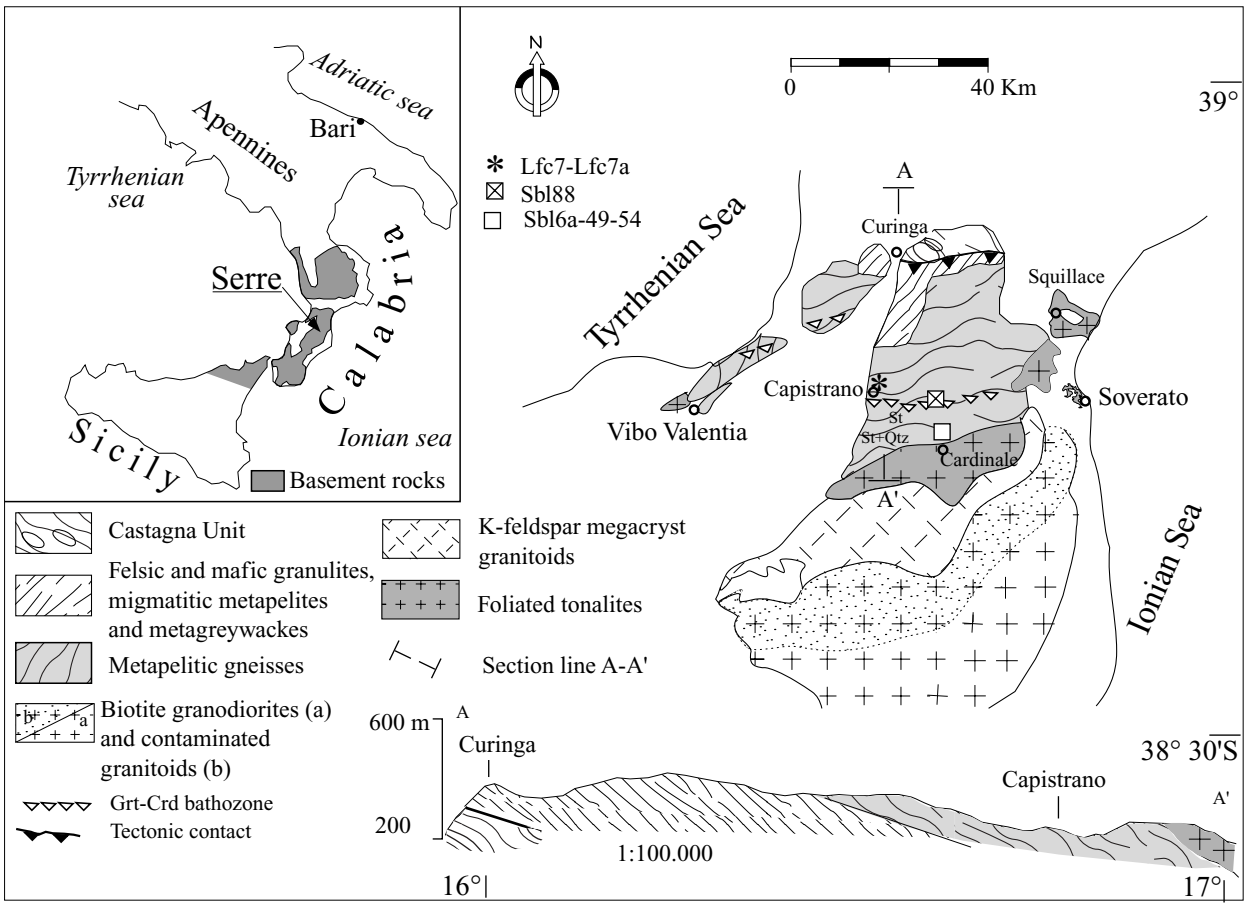

Figure 1. Geological sketch map and section of the Serre.

margins is still debated (e.g. Amodio Morelli *et al.* 1976; Bonardi *et al.* 1982; Dietrich, 1988; Bonardi *et al.* 2001). In Sila (northern Calabria) and in the Serre (southern Calabria), sections of the Hercynian lower continental crust crop out (e.g. Schenk, 1980, 1984; Caggianelli *et al*. 1991; Graessner & Schenk, 2001; Fornelli *et al*. 2002). These sections lie tectonically upon phyllonites of former amphibolite facies rocks (Castagna Unit, Fig. 1), which in turn overthrust a phyllitic unit (e.g. Colonna & Piccarreta, 1975; Paglionico & Piccarreta, 1976). The lower crustal sections are intruded by late Hercynian granitoids, which also intrude upper crustal low- to medium-grade metamorphic rocks (e.g. R. Dubois, unpub. Ph.D. thesis, Univ. Pierre et Marie Curie, 1976; Schenk, 1984; Ayuso *et al.* 1994; Graessner & Schenk, 2001; Caggianelli & Prosser, 2002) making up a nappe pile (Colonna, Lorenzoni & Zanettin Lorenzoni, 1973; Lorenzoni & Zanettin Lorenzoni, 1983; Borghi, Colonna & Compagnoni, 1992). The emplacement of granitoids at about 300 Ma was roughly synchronous with the metamorphic peak in the lower crustal sections (e.g. Schenk, 1980; Graessner & Schenk, 2001). Post-Hercynian metamorphic effects are mostly localized at the base of Sila and Serre lower crustal sections and in the middle part of the Serre section, where low-grade mylonites tens of metres to a hundred metres thick occur.

The lower crustal section of the Serre consists from bottom to top of metagabbros, felsic and mafic granulites, metapelites and some bodies of meta-ultramafites overlain by migmatitic metapelites and metagreywackes with minor metabasites and marbles. Available thermobarometry indicates: (1) *P–T*-peak conditions of 5.5–7.5 ± 0.5 kbar and 680–790 ± 30 °C at the top and bottom, respectively (e.g. Schenk, 1989, 1990) and (2) $P = 5.5$–6.5 kbar for the consolidation of the overlying foliated tonalites at Cardinale and Squillace (Fig. 1), respectively (Caggianelli, Prosser & Del Moro, 2000). A metamorphic zoning was recognized by Schenk (1984), who mapped 'Grt–Crd', 'staurolite' and 'St + Qtz' zones in the upper part of the section (Fig. 1). On the basis of textural evidence, the prograde evolution has been subdivided into an earlier kinematic stage and a subsequent static stage with heating outlasting the penetrative deformation; a rapid decompression of about 2 kbar and an isobaric cooling followed (Schenk, 1984).

Most of the rock-forming minerals, including Ky, St and Ms, show different textural characteristics, indicating that they had crystallized during prograde and retrograde stages of the metamorphic history.

https://doi.org/10.1017/S0016756805001482 Published online by Cambridge University Press

According to Fornelli *et al.* (2002), the metapelites underwent a multi-stage melting involving: (1) hydrous melting producing sodic and potassic melts, and (2) mica dehydration melting, under increasing T as well as under decreasing P, producing granitic melts which migrated far from the sources. The contribution of biotite to dehydration melting in the upper metapelites was limited by the lower temperatures they experienced and their generally higher Mg contents (Fornelli *et al.* 2004).

The mesosomes and melanosomes are more commonly strongly foliated with a prevalent planar texture defined by aligned biotite and sillimanite, within which porphyroblastic Grt (in the lower part) or Grt and Crd (in the upper part) occur. The principal foliation coincides at least with S_2 schistosity since at the outcrop and at thin-section scales, folds or hinges as well as folded trails of inclusions within the garnet are preserved (see also Kruhl & Huntemann, 1991). The highest grade mineral assemblages observed within metapelites are constituted mainly by the combination of Bt + Sil + Grt + Crd ± Qtz ±Pl ± Kfs ± Ilm/Rt in the upper part and of Grt + Sil + Rt/Ilm + Pl ± Kfs ± Bt in the lower part where Crd may also be present but not in Kfs-bearing assemblages (Schenk, 1984, 1990). High-strain zones post-dating the metamorphic peak and paralleling the S_2 schistosity are present in the upper part of the migmatitic metapelites and produce non-pervasive high-T mylonitic foliation (Fig. 2a). In these zones, quartz forms long ribbons, cordierite of the matrix is boudinaged, and garnet forms ribbons (Fig. 2a) showing dilatation fractures filled with Crd + Spl + Sil + Bt + Ilm (Fig. 2b). Interestingly, in a low-grade mylonite sampled near Squillace (Fig. 1), the open pull-aparts in the porphyroclastic sillimanite are filled with chloritoid (Fig. 2c). These microtextures suggest that the above high-strain zones formed both under high temperatures during the Hercynian evolution and also under low temperatures in post-Hercynian times. The high-T mylonites occur within the Crd–Grt bathozone (Fig. 1) near which a marble level crops out. Marble shows a complicated folding pattern and includes centimetric pieces of mylonitic Grt–Bt gneiss. The silicates (olivine, clinopyroxene) show deformation and fractures and carbonates of the matrix are recrystallized. On the whole these features seem to indicate characteristics of a shear zone (study in progress).

3. Sample description and analytical methods

The present paper deals with the detailed study of the migmatitic metapelites straddling the 'Grt–Crd bathozone' along a NW–SE-oriented profile (Fig. 1).

We have studied more than one hundred thin-sections and have selected six samples for mineral analyses. Three samples (Sbl6a, Sbl49, Sbl54) were collected several metres to about a hundred metres below the contact with the Cardinale tonalites; one sample (Sbl88) comes from about 5 km from the contact with the tonalites (Fig. 1) within the 'Crd–Grt bathozone' (Schenk, 1984), ~ 500–600 m deeper in the section. Two other samples (Lfc7 and Lfc7a) were taken at a lower structural level, just north of Capistrano (Fig. 1). Samples Sbl6a, Sbl49 and Sbl54 are referred to as 'shallower samples', whereas Sbl88, Lfc7A and Lfc7 are called 'deeper samples'. Sample Sbl88 is highly strained and contains the assemblage Bt–Grt–Crd–Kfs–Sil–Qtz and Rt–Ilm–Mnz–Zrn–Spl as accessories. The shallower samples are very rich in biotite and sillimanite with garnet and cordierite, and commonly lack K-feldspar in the restite. Some K-feldspar has been found in the sample Sbl6a within a Bt-rich layer (Fig. 3a). Samples Lfc7 and Lfc7a contain the assemblage Grt–Bt–Sil–Crd–Pl–Qtz. One- or two-feldspar leucosomes are present at thin-section and outcrop scales. They may contain garnet or cordierite or both; sillimanite is ubiquitous, whereas kyanite and staurolite are very rare (Fig. 2d). Staurolite, kyanite and muscovite are also present within the shallower samples both as relics and retrograde phases, whereas within the deeper samples only relict kyanite has been found (Sbl88). Late andalusite occurs within the shallower samples. Schenk (1984), however, reports the occurrence of retrograde andalusite and kyanite also in the univariant zone. Relict Ms, reported here for the first time, occurs as rare micrometric inclusions within Grt, Bt, Ky or as single small crystals within Bt-rich melanosomes.

Minerals were analysed on polished thin-sections using a Cambridge S360 electron microscope equipped with a LINK AN 10.000 Si (Li) energy dispersive detector. Operating conditions were 15 kV accelerating potential and a probe current of about 1 nA. EDS intensities were converted into wt % oxides by ZAF 4/FLS quantitative analysis software support. Conventional thermobarometric calculations were made by the GPT program 'An Excel spreadsheet for thermobarometric calculations in metapelitic rocks' by Reche & Martinez (1996). The average P–T for each sample was calculated using the Thermocalc 3.25 program (Powell & Holland, 1994).

4. Chemistry and textures of minerals

The interiors of Grt, Crd and Bt are commonly homogenized, implying a residence time at high T sufficient to obliterate or attenuate the original growth zoning through intracrystalline diffusion.

Biotite defines the fabric; it forms inclusions in garnet and also symplectitic aggregates with quartz and feldspars suggestive of its involvement in the melting reactions; it is also one of the products replacing garnet and cordierite. Biotite may include staurolite, kyanite and, very rarely, relict muscovite (Fig. 3a, b). The retrograde Bt replacing Crd is greenish and is

https://doi.org/10.1017/S0016756805001482 Published online by Cambridge University Press

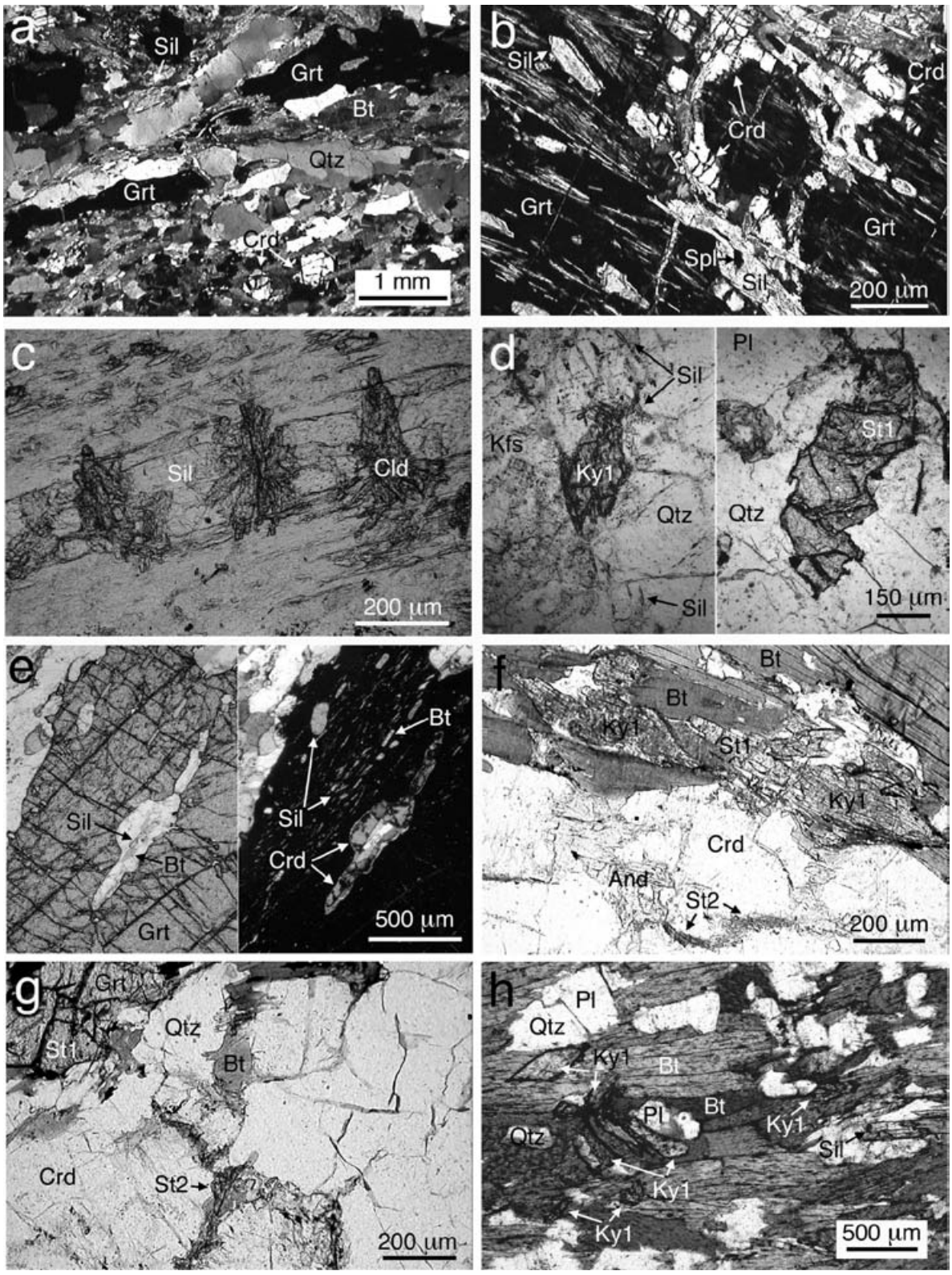

Figure 2. Microfabrics of the studied migmatites. (a) High-*T* mylonitic fabric showing ribbons of Grt (Sbl88). Crossed polarized light. (b) Pull-apart in a ribbon of Grt (Sbl88): Crd corona around a fragment of Grt and remnants of Spl within Sil. Crossed polarized light. (c) Greenschist-facies mylonite showing dilatation fractures in porphyroclastic Sil filled with 'rosettes' of chloritoid. Plane polarized light. (d) Relict kyanite (Ky_1) and staurolite (St_1) in the quartz-feldspar aggregate in a granitic leucosome from the shallower part of the studied profile. Plane polarized light. (e) Symplectite Crd–Qtz (crossed polarized light on right, plane polarized light on left) including Bt, Rt and resorbed Sil in the outer core of a garnet porphyroblast showing a rim including Sil, Pl, Bt and some Crd (Crd–Grt zone). (f) St_1 protected by deformed Ky_1 and Bt along the foliation and late formation of St_2 and And from Crd within the shallower samples. Plane polarized light. (g) Straight contact between St_1 and Grt and late formation of St_2 (shallower sample). Plane polarized light. (h) Relict kyanite (Ky_1) along the foliation and defining the hinge of a microfold (in a shallower sample). Plane polarized light.

https://doi.org/10.1017/S0016756805001482 Published online by Cambridge University Press

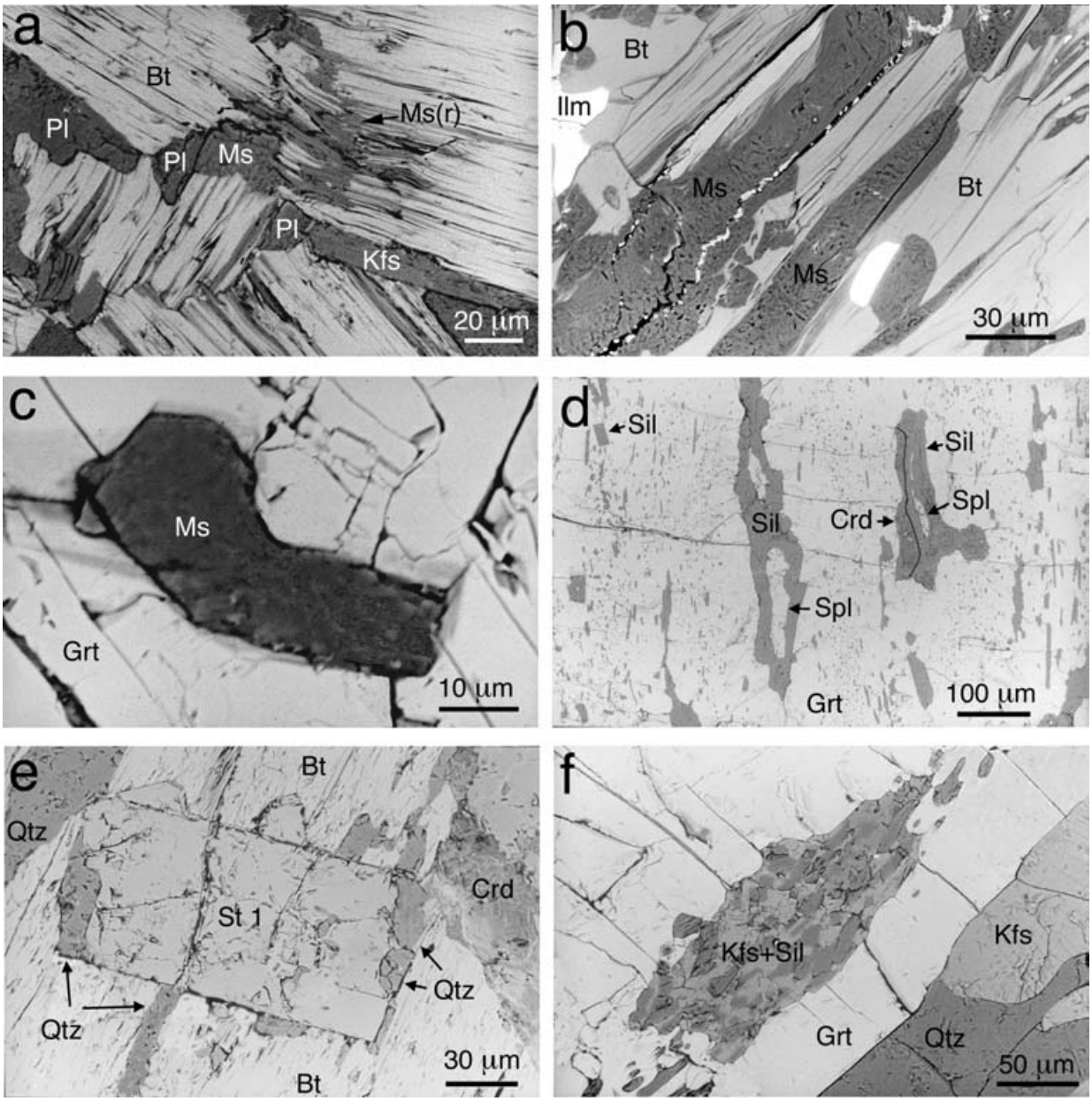

Figure 3. SEM photographs showing significant textures in the studied migmatites. (a) Deformed flakes of relict Ms ($Si_{11ox} = 3.26$) between deformed Bt-crystals (with Pl and Kfs) and undeformed retrograde Ms(r) ($Si_{11ox} = 3.07$) along the cleavage of the deformed Bt (Sbl6a); (b) relict Ms ($Si_{11\ ox} = 3.29$) within Bt of a residual layer (Sbl6a); (c) relict Ms ($Si_{11ox} = 3.17$) in a resorbed garnet (Sbl6a); (d) coronitic microdomains within a ribbon of Grt interpreted as a result of reaction Grt + Sil = Crd + Spl followed by regrowth of Sil (Sbl88); (e) euhedral St_1 within Bt of the foliation (Sbl54a); (f) aggregate of Kfs + Sil within Grt in contact with K-feldspar (Sbl88) indicating reaction (5).

characterized by very low Ti/11ox contents (0.02–0.03) and by low X_{Fe} (0.36–0.37). The reddish biotite of the fabric tends to be homogeneous in X_{Fe} but not in Ti in each sample (Table 1, Fig. 4). In samples Sbl6a and Sbl49, Bt composition in the matrix and within the garnet or plagioclase is substantially the same, with X_{Fe} in the range 0.49–0.55, and Ti/11ox ranging from 0.10 to 0.20 (Table 1, Fig. 4); the analysed Bt in contact with resorbed Grt falls in the same compositional range close to the highest values. The biotite in the matrix of sample Sbl54 has lower contents of Fe ($X_{Fe} = 0.34$–0.36) and of Ti/11ox (0.07–0.13) (Fig. 4). In the deeper samples (Sbl88, Lfc7 and Lfc7a), Bt in the matrix has the lowest X_{Fe} (0.27–0.35, Table 1) and Ti/11ox values mostly from 0.22 to 0.28 (Fig. 4); Bt included in the Grt has Ti/11ox content even higher (up to 0.39, not reported in Fig. 4); Bt included in Pl has X_{Fe} around 0.31 and Ti/11ox value of 0.26 (Table 1). A compositional gap appears between the shallower and deeper samples (Fig. 4).

https://doi.org/10.1017/S0016756805001482 Published online by Cambridge University Press

Table 1. Representative biotite analyses in the samples of the studied segment (formula on the basis of 22 oxygens)

	Deeper samples					Shallower samples												
Sample	Lfc7	Lfc7	Lfc7a	Sbl88	Sbl88	Sbl6a	Sbl6a	Sbl6a	Sbl6a	Sbl6a	Sbl6a	Sbl6a	Sbl49	Sbl49	Sbl49	Sbl49	Sbl54	Sbl54
Spot	105 in matrix	106 in matrix	144 in Grt	73 in Pl	80 in matrix	53 in Pl	92 adjacent Pl	95 in Pl	106 in Pl	149 adjacent Grt	151 adjacent Grt	153 adjacent Grt	83 in matrix	84 in matrix	168 in matrix	169 rim in matrix	62 core in matrix	64 in matrix
SiO_2	37.17	36.95	36.32	37.33	36.94	35.89	35.12	35.85	35.73	35.46	35.33	34.87	35.92	35.63	35.66	36.04	37.41	37.76
TiO_2	4.73	5.15	5.31	4.78	4.49	3.12	1.69	1.86	3.25	2.37	2.89	2.22	2.72	3.54	2.24	2.27	1.23	1.37
Al_2O_3	17.26	17.14	17.29	16.88	16.93	20.21	19.37	19.64	20.06	19.85	20.11	19.39	19.13	19.19	19.51	19.57	20.18	19.88
FeO	11.27	11.59	11.91	11.89	13.52	18.71	19.99	19.13	18.31	19.79	18.73	20.44	18.88	18.75	18.42	18.08	13.78	13.70
ZnO	0.00	0.00	0.00	0.00	0.22	0.00	0.00	0.35	0.35	0.00	0.00	0.31	0.00	0.00	0.00	0.31	0.25	0.00
MgO	16.02	15.86	15.36	15.07	14.09	8.81	10.17	9.74	8.49	8.74	9.21	9.09	9.67	9.37	10.47	10.42	14.02	14.25
K_2O	9.78	9.70	9.63	10.15	9.71	9.60	9.54	9.73	9.55	10.01	9.63	9.87	9.75	9.86	9.89	9.50	9.29	8.65
Total	96.23	96.39	95.82	96.10	95.90	96.34	95.88	96.30	95.74	96.22	95.90	96.19	96.07	96.34	96.19	96.19	96.16	95.61
Si	5.397	5.367	5.320	5.454	5.446	5.367	5.329	5.395	5.379	5.360	5.320	5.308	5.406	5.352	5.355	5.392	5.455	5.503
Ti	0.516	0.563	0.585	0.525	0.498	0.351	0.193	0.210	0.368	0.269	0.327	0.254	0.308	0.400	0.253	0.255	0.135	0.150
Al	2.954	2.934	2.985	2.907	2.942	3.562	3.464	3.483	3.559	3.536	3.569	3.479	3.393	3.398	3.453	3.451	3.468	3.415
Al^{IV}	2.603	2.633	2.680	2.546	2.554	2.633	2.671	2.605	2.621	2.640	2.680	2.692	2.594	2.648	2.645	2.608	2.545	2.497
Al^{VI}	0.351	0.301	0.305	0.361	0.388	0.929	0.793	0.878	0.938	0.896	0.889	0.787	0.799	0.750	0.808	0.843	0.923	0.916
Fe^{2+}	1.369	1.408	1.459	1.453	1.667	2.340	2.537	2.407	2.305	2.502	2.359	2.602	2.376	2.356	2.313	2.262	1.680	1.670
Zn	0.000	0.000	0.000	0.000	0.024	0.000	0.000	0.039	0.039	0.000	0.000	0.035	0.000	0.000	0.000	0.034	0.027	0.000
Mg	3.468	3.434	3.354	3.282	3.097	1.964	2.300	2.185	1.905	1.970	2.068	2.063	2.170	2.098	2.344	2.324	3.048	3.096
K	1.812	1.797	1.800	1.892	1.826	1.832	1.847	1.868	1.834	1.930	1.850	1.917	1.872	1.890	1.895	1.813	1.728	1.608
Σcat.	15.515	15.502	15.502	15.513	15.499	15.416	15.670	15.587	15.390	15.567	15.493	15.657	15.525	15.494	15.613	15.533	15.540	15.443
X_{Fe}	0.283	0.291	0.303	0.307	0.350	0.544	0.524	0.524	0.548	0.559	0.533	0.558	0.523	0.529	0.497	0.493	0.355	0.350
Ti/11	0.258	0.282	0.292	0.262	0.249	0.176	0.097	0.105	0.184	0.134	0.163	0.127	0.154	0.200	0.126	0.127	0.068	0.075

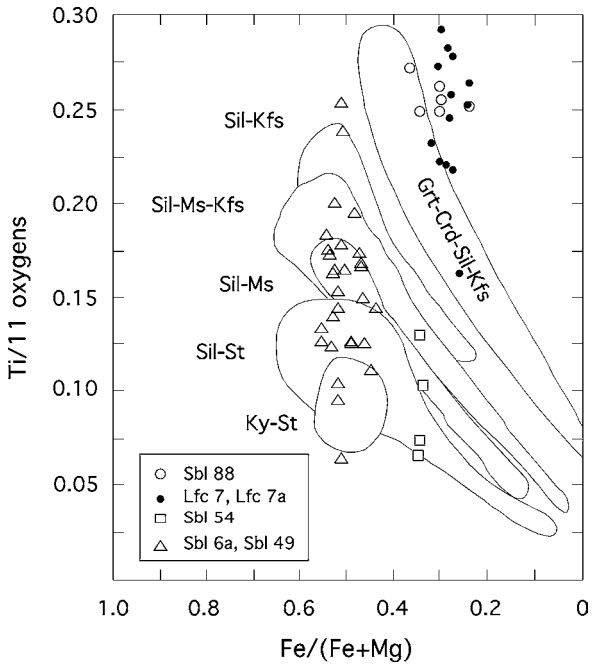

Figure 4. X_{Fe} v. Ti_{11ox} plot for biotite. Triangles: shallower samples (Sbl6a, Sbl49); squares: shallower sample sbl54; open (Sbl88) and closed (Lfc7, Lfc7A) circle: deeper samples. Unshaded fields: compositional ranges of biotite from metamorphic zones in New England (Robinson *et al*. 1982).

Garnet forms large (up to 1 cm) and small (submillimetric) crystals. The former might be subhedral or resorbed. In highly strained migmatites, garnets are lenticular and may be elongated (Fig. 2a); it is frequently crushed or shows parallel fractures perpendicular to the foliation. Within the shallower samples, it may be inclusion-free or includes Bt, Bt + Pl, Bt + Sil ± Pl ± Qtz, Ilm and Crd. SEM observation of resorbed porphyroblasts of garnet without inclusions of Al-silicate (Sbl6a) indicates one inclusion of Ms having straight contacts with garnet (Fig. 3c). Within the deeper samples, garnet includes Sil, Bt, Pl, Rt, Ilm and Crd (Fig. 2e). The highly strained sample Sbl88 contains ribbons of garnet (up to 15 × 2 mm) with dilatation fractures (Fig. 2b). One ribbon shows a central band homogeneously rich in fibrolite, and symmetrical outer portions in which fibrolite forms small lenses. It includes biotite flakes smaller than those of the matrix, ilmenite and rutile rimmed by ilmenite. Within the fibrolite-rich part and the open fractures, there are 'coronitic microdomains' which consist of (1) Spl rimmed by Sil with or without an outer shell of Crd within garnet (Fig. 3d), and (2) Crd rimming fragments of Grt or including Sil which hosts Spl (Fig. 2b), Rt rimmed by Ilm and red Bt as infill of the pull-apart.

Garnets tend to have quasi-homogeneous interiors and narrow retrograde rims. X_{Fe} ranges from 0.60 to 0.90 (Tables 2, 3) and X_{Mn} increases in the rim. Grt of sample Sbl6a (the shallowest) documents the highest contents of Sps 8.2–15.0 % in the core and 13.4–16.8 % in the rim (Table 3; Fig. 5). In samples Sbl6a and Sbl49, garnet X_{Fe} ranges from 0.79 to 0.87 in the interiors and from 0.85 to 0.90 in the rims, whereas in sample Sbl54, Grt has lower X_{Fe} and Sps content (Table 3). Sample Sbl88 contains crystals having different compositions (Table 2): (1) one very small crystal included in Sil

Table 2. Representative garnet analyses in the deeper samples of the studied segment (formula on the basis of 12 oxygens)

Sample	Lfc7	Lfc7	Lfc7	Lfc7	Lfc7a	Sbl88	Sbl88	Sbl88	Sbl88	Sbl88	Sbl88
Spot	97*	98*	99*	136	141	69*	70*	71*	77	82	124
	core	rim	rim	core	core	core	outer core	rim	core in Sil	rim	rim
SiO_2	38.39	39.57	38.87	38.98	37.96	38.69	38.40	38.52	39.62	38.12	39.11
TiO_2	0.00	0.00	0.00	0.00	0.00	0.00	0.00	0.00	0.00	0.00	0.00
Al_2O_3	22.33	22.63	22.48	22.61	22.24	22.15	21.95	22.01	22.82	21.54	22.10
FeO	27.63	27.00	27.91	28.06	27.56	29.03	30.09	29.96	27.28	33.70	29.41
ZnO	0.00	0.00	0.00	0.00	0.00	0.35	0.00	0.00	0.00	0.33	0.12
MnO	0.00	0.47	0.39	0.48	0.59	0.22	0.12	0.55	0.12	0.28	0.28
MgO	9.83	9.69	9.72	9.77	8.95	8.28	7.86	7.82	9.27	4.85	8.16
CaO	1.43	1.58	1.43	1.35	1.94	1.41	1.39	1.36	1.60	1.27	1.43
Total	99.61	100.94	100.80	101.25	99.24	100.14	99.85	100.28	100.78	100.12	100.61
Si	2.962	3.000	2.968	2.964	2.954	2.993	2.991	2.990	3.008	3.018	3.010
Ti	0.000	0.000	0.000	0.000	0.000	0.000	0.000	0.000	0.000	0.000	0.000
Al	2.030	2.022	2.023	2.026	2.040	2.020	2.015	2.014	2.042	2.010	2.005
Fe^{2+}	1.783	1.712	1.782	1.784	1.794	1.878	1.960	1.945	1.732	2.231	1.893
Zn	0.000	0.000	0.000	0.000	0.000	0.020	0.000	0.000	0.000	0.019	0.007
Mn	0.000	0.030	0.025	0.031	0.039	0.014	0.008	0.036	0.008	0.019	0.018
Mg	1.131	1.095	1.106	1.107	1.038	0.955	0.913	0.905	1.049	0.572	0.936
Ca	0.118	0.128	0.117	0.110	0.162	0.117	0.116	0.113	0.130	0.108	0.118
Σcat.	8.023	7.989	8.021	8.023	8.026	7.997	8.002	8.003	7.970	7.977	7.987
X_{Fe}	0.612	0.610	0.617	0.617	0.633	0.663	0.682	0.682	0.623	0.796	0.669
Sps	0.0	1.0	1.0	0.0	1.4	0.5	0.3	1.2	0.3	0.6	0.6
Alm	57.7	57.6	58.0	58.5	58.2	63.4	65.4	64.8	59.3	76.2	63.8
Prp	38.2	37.0	37.0	37.7	35.0	32.2	30.5	30.2	35.9	19.5	31.6
Grs	4.1	4.4	4.0	3.8	5.4	3.9	3.9	3.8	4.5	3.7	4.0

Spot with * in adjacent columns indicates analyses of the same crystal.

https://doi.org/10.1017/S0016756805001482 Published online by Cambridge University Press

Table 3. Representative garnet analyses in the shallower samples of the studied segment (formula on the basis of 12 oxygens)

Sample	Sbl6a	Sbl6a	Sbl6a	Sbl6a	Sbl6a	Sbl6a	Sbl6a	Sbl6a	Sbl6a	Sbl6a	Sbl6a	Sbl49	Sbl49	Sbl49	Sbl49	Sbl49	Sbl54	Sbl54	Sbl54
Spot	49 core	51* core	52* rim	97 core	103 rim	148 rim	150 rim	152 rim	157 core	202 core	204 core	85* core	86* rim	162 rim	167 core	170 core	127* core	128* rim	131 core
SiO_2	37.63	37.12	37.20	37.66	37.28	37.09	36.99	36.90	37.39	37.86	37.65	37.70	37.34	37.43	37.66	37.50	38.18	37.74	38.07
TiO_2	0.00	0.00	0.00	0.00	0.00	0.00	0.00	0.13	0.00	0.14	0.00	0.00	0.13	0.00	0.00	0.24	0.00	0.00	0.00
Al_2O_3	21.79	21.42	21.23	21.26	21.00	21.55	21.18	20.88	21.57	21.55	21.52	21.61	21.64	21.26	21.64	21.31	21.87	21.63	21.52
FeO	31.67	31.93	31.65	32.05	30.65	30.86	30.96	31.17	30.92	32.89	30.85	33.50	33.74	35.04	33.84	33.90	32.38	33.19	32.92
ZnO	0.28	0.25	0.26	0.00	0.00	0.00	0.44	0.00	0.38	0.00	0.00	0.17	0.00	0.00	0.00	0.32	0.00	0.45	0.21
MnO	4.67	3.78	6.16	4.66	6.77	7.11	6.92	7.04	5.93	3.63	6.52	2.47	3.25	3.24	1.36	2.97	1.27	1.10	1.09
MgO	3.46	3.47	2.87	3.41	2.02	2.43	2.57	2.45	3.02	3.88	2.78	4.00	2.95	2.37	4.59	3.24	5.71	5.19	5.43
CaO	1.13	1.34	1.06	1.20	1.51	1.16	1.29	1.22	1.14	1.06	1.30	1.07	1.29	1.24	1.15	1.24	1.27	1.29	0.97
Total	100.63	99.31	100.43	100.24	99.23	100.20	100.35	99.66	100.35	101.01	100.62	100.52	100.34	100.58	100.24	100.72	100.67	100.59	100.21
Si	2.994	2.993	2.991	3.012	3.029	2.988	2.985	2.998	2.995	2.998	3.008	2.997	2.990	3.007	2.991	2.994	2.993	2.982	3.007
Ti	0.000	0.000	0.000	0.000	0.000	0.000	0.000	0.000	0.000	0.008	0.000	0.000	0.000	0.000	0.000	0.014	0.000	0.000	0.000
Al	2.044	2.036	2.012	2.004	2.011	2.046	2.014	1.999	2.037	2.011	2.026	2.025	2.042	2.013	2.025	2.005	2.021	2.014	2.003
Fe^{2+}	2.108	2.153	2.129	2.144	2.083	2.079	2.089	2.118	2.071	2.178	2.061	2.227	2.259	2.354	2.247	2.264	2.123	2.193	2.175
Zn	0.016	0.015	0.015	0.000	0.000	0.000	0.026	0.000	0.022	0.000	0.000	0.010	0.000	0.000	0.000	0.019	0.000	0.026	0.012
Mn	0.315	0.258	0.420	0.316	0.466	0.485	0.473	0.484	0.402	0.243	0.441	0.166	0.220	0.091	0.201	0.084	0.074	0.073	
Mg	0.410	0.417	0.344	0.407	0.245	0.292	0.309	0.297	0.361	0.458	0.331	0.474	0.352	0.284	0.543	0.386	0.667	0.611	0.639
Ca	0.096	0.116	0.091	0.103	0.131	0.100	0.112	0.106	0.098	0.090	0.111	0.091	0.111	0.107	0.098	0.106	0.107	0.109	0.082
Σcat.	7.984	7.989	8.002	7.986	7.965	7.989	8.008	8.002	7.987	7.988	7.979	7.991	7.982	7.986	7.996	7.989	7.996	8.011	7.991
X_{Fe}	0.837	0.838	0.861	0.840	0.895	0.877	0.871	0.877	0.852	0.826	0.862	0.825	0.865	0.892	0.805	0.854	0.761	0.782	0.773
Sps	10.8	8.8	14.1	10.6	15.9	16.4	15.9	16.1	12.3	8.2	15.0	5.6	7.5	7.4	3.1	6.8	2.8	2.5	2.5
Alm	71.9	73.1	71.4	72.2	71.2	70.3	69.9	70.5	70.7	73.4	70.0	75.2	76.7	79.4	75.4	76.5	71.2	73.4	73.2
Prp	14.0	14.2	11.5	13.7	8.4	9.9	10.4	9.9	13.7	15.4	11.2	16.1	12.0	9.6	18.2	13.1	22.4	20.5	21.5
Grs	3.3	3.9	3.0	3.5	4.5	3.4	3.8	3.5	3.3	3.0	3.8	3.1	3.8	3.6	3.3	3.6	3.6	3.6	2.8

Spot with * in adjacent columns indicate analyses of the same crystal.

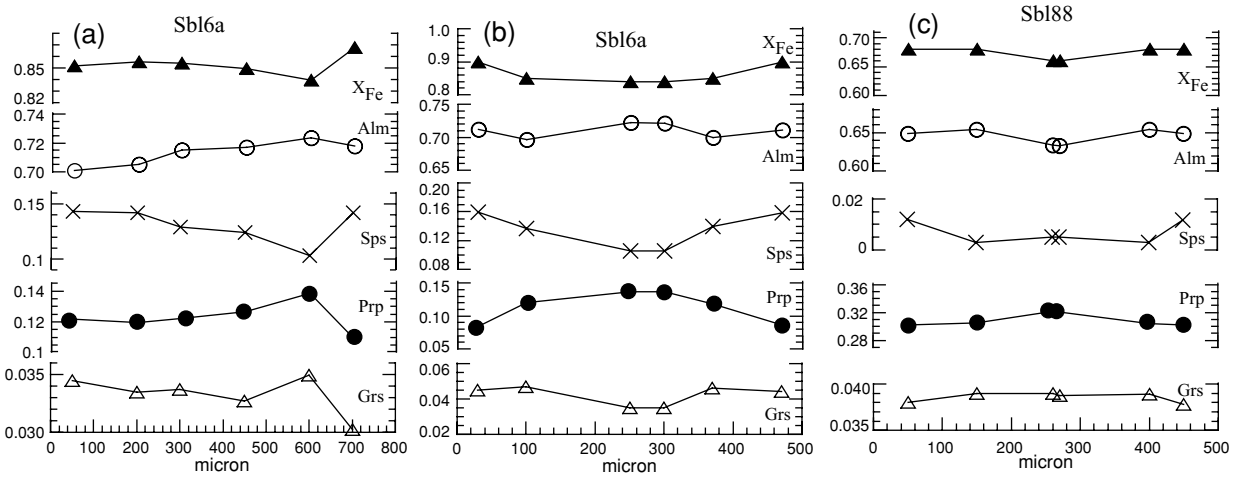

Figure 5. Profiles of Grt from metapelitic migmatites: (a) deeply resorbed garnet including Ms with $Si_{11ox} = 3.17$ (Sbl6a); (b) slightly symmetric zoning preserved in a garnet porphyroblast (Sbl6a); (c) profile of a garnet porphyroblast within the Crd–Grt zone (Sbl88).

shows the lowest Alm (59 %) and the highest Prp (36 %) contents; (2) elongated crystals show X_{Fe} ranging from 0.66 (core) to 0.68 (rim) (Fig. 5); (3) subhedral crystals show X_{Fe} from 0.72 (core) to 0.80 (rim). Samples Lfc7 and Lfc7a contain garnet having interiors with X_{Fe} 0.60 to 0.69.

The Grs contents are low and slightly increase or decrease in the rims (Tables 2–3, Fig. 5). On the whole, a compositional gap exists between the garnet of the deeper and shallower samples.

Cordierite occurs as porphyroblasts (up to 1–2 mm) and small crystals in the matrix, as inclusions in the peripheral part of the Grt (Fig. 2e) and as corona around it. The porphyroblasts of Crd and Grt of the matrix, when in contact, may show straight boundaries. In highly strained parts, cordierite in the matrix might be boudinaged. Samples from the Crd–Grt zone may show Crd–Qtz symplectite, including Bt, Rt and resorbed Sil in the periphery of porphyroblastic garnet (Fig. 2e), suggesting transition from Grt to Grt + Crd stability. Crd + Spl form from Grt reacting with Sil both inside the elongated crystals and the pull-apart (sample Sbl88; Figs 2b, 3d). In the shallower samples, Crd X_{Fe} averages 0.26 (Table 4); in sample Sbl88 it is around 0.20 in the matrix, the coronitic textures and dilatation fractures (Table 4); in sample Lfc7, X_{Fe} ranges from 0.14 to 0.17 (Table 4). Cordierite shows partial breakdown into sillimanite and andalusite-bearing assemblages (Fig. 2f), kyanite or staurolite (Fig. 2g), together with biotite, chlorite or muscovite (see also Schenk, 1984, 1990).

Muscovite has been found only within the shallower samples. It occurs: (1) as retrograde flakes filling engulfments of the resorbed Crd, or along the cleavage of Bt or as large crystals randomly distributed with respect to S_2; (2) as rare micrometric crystals within Grt and Bt or within an aggregate of Bt-crystals in

Table 4. Representative analyses of cordierite (formula on the basis of 18 oxygens)

Sample	Lfc7	Sbl88	Sbl88	Sbl54
Spot	100 in matrix	136* core	137* rim	63 in matrix
SiO_2	48.69	48.88	48.66	48.61
Al_2O_3	33.64	33.53	33.23	33.06
FeO	3.39	5.04	4.61	6.03
ZnO	0.00	0.00	0.23	0.00
MgO	11.91	10.80	10.80	9.83
Total	97.63	98.25	97.53	97.53
Si	4.939	4.961	4.971	4.990
Al	4.022	4.011	4.001	3.999
Fe^{2+}	0.288	0.428	0.394	0.518
Zn	0.000	0.000	0.017	0.000
Mg	1.801	1.634	1.645	1.504
Σcat.	11.050	11.034	11.028	11.011
X_{Fe}	0.138	0.208	0.193	0.256

Spot with * in adjacent columns indicate analyses of the same crystal.

melanosomic layers (Fig. 3a–c) and as rare and very small crystals within kyanite. The former type is clearly retrograde and, as in Sila (Graessner & Schenk, 2001), has low phengite contents (Si/11ox < 3.08 a.p.f.u.); the others are interpreted as relicts of the prograde stage and are richer in the phengite component (Table 5, Fig. 6): Si/11ox = 3.17–3.18 within the garnet, Si/11ox = 3.26–3.29 within or between flakes of biotite of the melanosomes. A Ms-bearing prograde stage has also been inferred on the basis of microtectonic characteristics and of inclusions in garnet from the migmatites of Catena Costiera (Piluso & Morten, 2004).

Retrograde Ms is also chemically distinguishable from the relict one by higher Ti and low Mg–Fe contents (Fig. 6). The variable phengite contents of white mica in the diverse structural positions, within the same thin-section, likely indicate growth

https://doi.org/10.1017/S0016756805001482 Published online by Cambridge University Press

Table 5. Representative analyses of muscovite (formula on the basis of 22 oxygens)

Sample	Sbl6a	Sbl6a	Sbl6a	Sbl6a	Sb16a	Sbl6a	Sbl6a
Spot	96 in Grt	159 adjacent Grt	14 in Bt	56 in Bt	10 retrogr.	186 adjacent Bt	189 in Grt
SiO_2	48.31	48.13	49.79	49.74	46.86	49.96	47.84
TiO_2	0.00	0.26	0.20	0.48	1.30	0.10	0.17
Al_2O_3	33.54	30.71	31.58	29.04	35.45	32.82	33.71
FeO	3.26	4.12	2.04	4.29	1.09	1.83	3.48
ZnO	0.00	0.00	0.00	0.00	0.30	0.00	0.00
MnO	0.20	0.00	0.00	0.00	0.00	0.00	0.00
MgO	0.89	2.26	1.57	3.16	0.45	1.58	0.71
K_2O	10.55	10.25	9.90	9.96	10.67	10.19	10.40
Total	96.75	95.73	95.08	96.67	96.12	96.48	96.31
Si	6.369	6.445	6.596	6.584	6.175	6.534	6.335
Ti	0.000	0.026	0.020	0.048	0.129	0.010	0.017
Al^{IV}	1.631	1.555	1.404	1.416	1.825	1.476	1.665
Al^{IV}	3.581	3.292	3.527	3.115	3.681	1.473	1.074
Fe^{2+}	0.359	0.461	0.226	0.475	0.120	0.200	0.385
Zn	0.000	0.000	0.000	0.000	0.029	0.000	0.000
Mn	0.022	0.000	0.000	0.000	0.000	0.000	0.000
Mg	0.175	0.451	0.310	0.624	0.088	0.308	0.140
K	1.774	1.751	1.673	1.682	1.794	1.698	1.757
Σcat.	13.912	13.981	13.756	13.943	13.841	13.790	13.896
X_{Fe}	0.672	0.505	0.422	0.432	0.577	0.394	0.733
Si/11	3.184	3.223	3.298	3.292	3.088	3.262	3.168

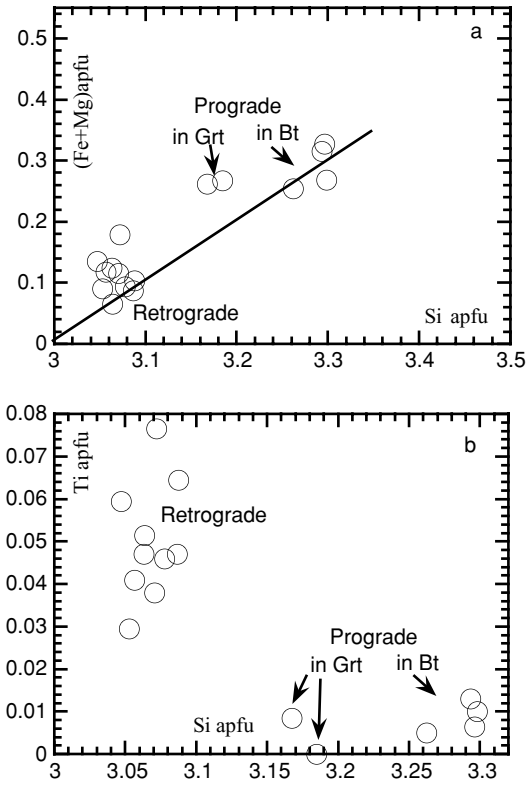

Figure 6. Chemical compositions of muscovite. Si against Fe + Mg (a) and Ti (b) (cations on 11 ox). The line of phengite substitution is indicated in (a).

under different physical conditions (e.g. Massonne & Schreyer, 1987).

Sillimanite occurs in the hinges of microfolds transposing S_1 into S_2, as coarse-grained prismatic crystals along or cross-cutting the S_2 foliation, as fibrolitic to prismatic inclusions in Grt (Fig. 2e) and Crd, and as retrograde products replacing Grt and Crd. In the highly strained portions the elongated crystals show undulations and open fractures filled with Bt or Chl.

Kyanite was found in melanosomes and mesosomes and, very rarely, also in leucosomes. It becomes more frequent and coarse-grained towards the uppermost part of the investigated section. Within the melanosomes and mesosomes it occurs in the main foliation as crystals deformed against staurolite (Ky_1 in Fig. 2f), wrapped by Bt and Sil and, locally, defining the hinges of microfolds (Fig. 2h). They show sharp contact with or form inclusions in the reddish biotite distributed along S_2 and might include drop-like quartz or very small crystals of Ms (very rarely) or of reddish Bt (more frequently); intergrowths with rutile rimmed by ilmenite occur along the mylonitic foliation in sample Sbl88. Kyanite crystals are also associated with greenish biotite and/or chlorite or retrograde muscovite around or in the vicinity of the resorbed cordierite (see also Schenk, 1990). In the leucosomes, kyanite forms single resorbed crystals in the quartz-feldspar aggregate (Fig. 2d) or clusters within a greenish Ti-poor biotite replacing Crd. The kyanite around cordierite is a retrograde phase which in the melanosomes and mesosomes might be associated with Mg-chlorite + andalusite, with textural evidence indicating it formed later than andalusite (see also Schenk, 1990). Kyanite occurring within the hinges of microfolds, as inclusions in biotite along S_2 or in the quartz-feldspar aggregate of leucosomes, is a relict phase.

Staurolite has been found rarely in the leucosomes (Fig. 2d). In melanosomes it occurs in close association

https://doi.org/10.1017/S0016756805001482 Published online by Cambridge University Press

Table 6. Representative plagioclase analyses in the samples of the studied segment (formula on the basis of 8 oxygens)

	Deeper samples									Shallower samples											
Sample	Lfc7	Lfc7	Lfc7	Lfc7	Lfc7	Lfc7a	Sbl88	Sbl88	Sbl88	Sbl6a	Sbl6a	Sbl6a	Sbl6a	Sbl6a	Sbl6a	Sbl6a	Sbl49	Sbl49	Sbl49	Sbl49	Sbl54
Spot	103 core adjacent Grt	109* core in matrix	110* rim in matrix	111 rim	118 core in matrix	161 core in matrix	120 rim adjacent Grt	121 core in matrix	123 rim adjacent Grt	93 rim	100 core	104* core in Grt	105* rim	155 core	200 core in matrix	207 core in matrix	87 core adjacent Grt	163* rim	164* core	172 core	129 core
SiO_2	56.69	57.05	57.37	57.79	56.85	57.38	58.28	58.36	58.49	61.20	60.63	61.76	58.44	58.69	60.10	60.43	58.52	59.19	58.18	58.86	58.69
Al_2O_3	26.93	27.08	27.10	26.69	27.76	27.53	26.00	26.48	25.99	24.57	25.21	23.72	25.62	25.90	24.60	24.81	25.91	25.99	25.94	26.01	25.90
CaO	7.93	8.31	8.23	8.32	8.50	8.19	7.90	8.13	7.60	5.70	6.48	4.62	7.44	7.20	6.20	5.97	7.38	7.38	7.59	7.63	7.20
Na_2O	7.49	7.19	7.63	7.36	7.15	7.83	7.44	7.43	7.68	8.78	8.40	8.69	7.55	7.94	8.59	8.54	7.86	7.66	7.80	7.60	7.94
K_2O	0.28	0.00	0.15	0.19	0.16	0.00	0.00	0.16	0.00	0.00	0.00	0.66	0.55	0.00	0.00	0.00	0.04	0.13	0.00	0.00	0.00
BaO	0.15	0.00	0.00	0.00	0.18	0.00	0.24	0.00	0.00	0.00	0.15	0.00	0.00	0.00	0.00	0.00	0.10	0.00	0.00	0.00	0.00
Total	99.47	99.63	100.48	100.35	100.90	100.93	99.86	100.56	99.76	100.25	100.87	99.45	99.60	99.73	99.49	99.75	99.81	100.35	99.51	100.10	99.73
Si	2.562	2.566	2.565	2.558	2.541	2.553	2.615	2.600	2.621	2.713	2.680	2.756	2.629	2.629	2.691	2.695	2.624	2.634	2.616	2.627	2.629
Al	1.435	1.436	1.428	1.445	1.462	1.444	1.375	1.391	1.373	1.284	1.313	1.248	1.359	1.367	1.298	1.304	1.369	1.363	1.375	1.368	1.367
Ca	0.384	0.401	0.394	0.395	0.407	0.390	0.380	0.388	0.365	0.271	0.307	0.221	0.359	0.346	0.297	0.285	0.355	0.352	0.366	0.365	0.346
Na	0.656	0.627	0.661	0.632	0.620	0.675	0.647	0.642	0.667	0.755	0.720	0.752	0.659	0.690	0.746	0.738	0.683	0.661	0.680	0.658	0.690
K	0.016	0.000	0.009	0.011	0.009	0.000	0.000	0.009	0.000	0.000	0.000	0.038	0.032	0.000	0.000	0.000	0.002	0.007	0.000	0.000	0.000
Ba	0.003	0.000	0.000	0.000	0.009	0.000	0.000	0.004	0.000	0.000	0.003	0.000	0.000	0.000	0.000	0.000	0.002	0.000	0.000	0.000	0.000
Σcat.	5.056	5.056	5.056	5.040	5.040	5.042	5.038	5.021	5.030	5.022	5.023	5.015	5.037	5.032	5.033	5.022	5.035	5.018	5.037	5.018	5.032
Ab	62.1	61.0	62.2	60.9	59.8	63.4	63.0	61.8	64.6	73.6	70.1	74.4	62.8	66.6	71.5	72.1	65.7	64.8	65.0	64.3	66.6
An	36.4	39.0	37.0	38.1	39.3	36.6	37.0	37.4	35.4	26.4	29.9	21.9	34.2	33.4	28.5	27.9	34.1	34.5	35.0	35.7	33.4
Or	1.5	0.0	0.8	1.0	0.9	0.0	0.0	0.9	0.0	0.0	0.0	3.7	3.0	0.0	0.0	0.0	0.2	0.7	0.0	0.0	0.0

Spot with* in adjacent columns indicate analyses of the same crystal.

with relict kyanite (Ky_1 and St_1, respectively, in Fig. 2d, f) and shows different textures: (1) inclusions in the red biotite aligned along the present foliation (St_1 in Fig. 3e), in microdomains including kyanite, inclusion-free garnet or garnet including Bt, Pl and Qtz; (2) larger crystals with worm-like quartz wrapped by Bt and Sil of the foliation or rimmed by Bt + Sil + Qtz + opaques; (3) seams of small crystals or larger anhedral to euhedral crystals around the resorbed cordierite (St_2 in Fig. 2f, g; see also Schenk, 1984). Staurolite has been observed within Pl (Fig. 2d) in the same leucosome which contains also the relict Ky. It shows X_{Fe} 0.75–0.80 and ZnO contents 1.68–3.42. Staurolite replacing cordierite and biotite is clearly retrograde (St_2), whereas staurolite included in biotite of the foliation (Fig. 3e) and most of that distributed as single crystals or in clusters along the S_2 foliation, as well as that occurring in leucosomes, is interpreted as a relict phase.

Plagioclase ranges in composition from An_{40} to An_{32} (Table 6) in the highest grade rocks (Sbl88, Lfc7 and Lfc7a), whereas some crystals included in garnet have $An_{42–49}$. In the shallower samples, plagioclase composition ranges from An_{22} to An_{30} (Table 6) with the exception of a few extreme compositions (An_{55} and An_{11}). Plagioclase in contact with garnet may show slightly higher An content than in its core and one small crystal included in the garnet of sample Sbl6a (Table 6) shows a strong An enrichment towards the rim (from An_{22} to An_{34}).

5. *P–T–t* path

5.a. Prograde metamorphic stage

The first evidence for the *P–T* conditions attained during the metamorphic evolution of the studied migmatites is given by the observed mineral assemblages, reaction textures, mineral compositions and inclusions. High-*T* peak is supported by the prograde Ms–Bt-dehydration melting and the general absence of primary Ms. Decompression appears from Crd replacing Grt, and cooling at low *P* is evident from Sil–And–Ky progressive formation.

The shallower samples preserve memory of prograde stages: Ms (Si/11ox = 3.17–3.18) as single crystals included in garnet (Fig. 3c); St in straight contact with Grt (St_1 in Fig. 2g); deformed crystals of Ky in the hinges of microfolds or protecting undeformed St along the foliation (Ky_1 and St_1 in Fig. 2f, h); small inclusions of Ms or Qtz or of Bt within the Ky_1; relict Ms with Si/11ox = 3.26–3.29 in biotite-rich restitic layers (Fig. 3a, b); relict St and Ky included in quartz-feldspar aggregate of Sil-bearing leucosomes (Fig. 2d); multi-stage melting starting from H_2O-fluxed melting and progressing through dehydration melting of micas under increasing temperatures (Fornelli *et al*. 2002). Grt–Bt–Ms–Ky–Pl–Qtz–Ilm was the likely assemblage before the partial melting.

The Ms (Si/11ox = 3.17–3.18) armoured within porphyroblastic garnet without inclusions of Al-silicate (Sbl6a) suggests *P* of about 4–5 kbar at *T* around 500 °C (Massonne *in* Brouwer, Vissers & Lamp, 2002). This pressure estimate should theoretically be regarded as a minimum value since the microdomain lacks Kfs and does not contain the limiting assemblage (Massonne & Schreyer, 1987). After the growth of some Grt, the formation of St_1 and Ky_1 might be speculatively described as consequences of the following reactions under prograde conditions:

$$\text{Grt} + \text{Chl} + \text{Ms} = \text{St}_1 + \text{Bt} + \text{V} \quad (1)$$

$$\text{St}_1 + \text{Chl} + \text{Ms} = \text{Ky}_1 + \text{Bt} + \text{V} \quad (2)$$

The small inclusions of Ms or Qtz and of Bt within the relict kyanite, suggest the reaction:

$$\text{phengitic Ms} + \text{Qtz} = \text{Ky}_1 + \text{Bt} \quad (3)$$

The relict Ms with higher Si/11 ox (3.26–3.29), occurring within Bt or between crystals of Bt (Sbl6a), in Bt-rich restite is likely to post-date Ms (Si/11ox = 3.17–3.18) armoured in Grt (in the same thin-section) and to pre-date partial melting. This appears to be in agreement with the observation that the stability of Ms + Qtz in the uppermost metapelites was overstepped during the late stages of prograde metamorphic evolution (Schenk, 1990).

The occurrence of relict kyanite within both the melanosomes and sillimanite-bearing leucosomes suggests that the Ky–Sil transition occurred before melting started at *T* around 700 °C, that is, at *P* around 7 kbar. Ms with Si/11 ox = 3.26 occurs together with Bt, Pl and Kfs (Fig. 3a); the significance of Kfs, however, is not clear. It may be a relict of an earlier assemblage (together with Ms and part of Bt) or a product of the mica-dehydration melting. In any case, the Si content of the white mica suggests, theoretically, a minimum *P* around 8 kbar (Massonne *in* Brouwer, Vissers & Lamp, 2002), earlier than partial melting developed in the stability field of sillimanite.

Experimental works on partial melting of metapelites give further constraints. Garcìa-Casco *et al*. (2003) show that during the H_2O-fluxed melting of metapelites lacking Kfs, staurolite forms as a peritectic phase at *T* = 675–700 °C under *P* of 6–10 kbar near the Ky–Sil boundary (see also Thompson & Connolly, 1995). The possibility can thus not be ruled out that part of the relict staurolite in the melanosomes might be regarded as a peritectic phase during the hydrous melting left behind by segregating melts and survived during mica dehydration melting. Patiño Douce & Harris (1998) show that H_2O-fluxed melting at 6–10 kbar producing sodic melts (like many of the leucosomes in the studied migmatites: Fornelli *et al*. 2002) occurs before mica dehydration melting, and is favoured by higher pressure.

https://doi.org/10.1017/S0016756805001482 Published online by Cambridge University Press

Ms- and Bt-dehydration melting followed at $T =$ 700 °C, through the reactions

$$\text{phengitic Ms} + \text{Pl} + \text{Qtz} = \text{Bt} + \text{Kfs} + \text{Sil} + \text{melt} + \text{Ca-richer Pl} \quad (4)$$

$$\text{Bt} + \text{Sil} + \text{Qtz} + \text{Pl} = \text{Grt} + \text{Kfs} + \text{melt} \quad (5)$$

as indicated by the occurrence of K-feldspar, garnet and/or cordierite in some leucosomes. Cordierite might be produced instead of garnet by a melting reaction analogous to reaction (5) in Mg-rich metapelites (Spear, Kohn & Cheney, 1999). The $X_{Fe} \approx 0.80$ of Grt-cores indicates T of about 730 °C using the Grt isopleths calculated by Spear, Kohn & Cheney (1999) in the dehydration melting caused by reaction (5). Among the deeper samples, Sbl88 records information about a part of the prograde evolution which can be retrieved from the occurrence of relict Ky + Rt intergrowths along the foliation, Rt + Sil included in Grt and melting reaction (5), documented in Figure 3f. Partial melting continued until the univariant reaction

$$\text{Bt} + \text{Sil} + \text{Qtz} + \text{Pl} = \text{Grt} + \text{Crd} + \text{Kfs} + \text{melt} \quad (6)$$

was crossed. The $X_{Fe} = 0.62$–0.66 of Grt cores suggests T of about 780 °C and P of about 6 kbar when reaction (6) developed (Spear, Kohn & Cheney, 1999). Because of the textural relationships between Grt and Crd, we assume that reaction (6) occurred under decompression. This is in contrast with previous interpretations (Schenk, 1984, 1990; Graessner & Schenk, 2001) considering that the formation of the Grt + Crd + Bt + Sil + Qtz + Kfs assemblage records *P–T* peak conditions in Serre and Sila migmatites.

Crd–Spl and Ilm–Rt assemblages (Figs 2b, 3d) within Grt and Ilm including symplectitic Grt + Rt + Al-silicate are indicative of the garnet-consuming reactions

$$\text{Grt} + \text{Rt} = \text{Sil} + \text{Qtz} + \text{Ilm} \quad (7)$$

$$\text{Grt} + \text{Sil} = \text{Crd} + \text{Spl} \quad (8)$$

suggesting decompression.

5.b. Retrograde stage

The Crd-corona around Grt suggests the reaction

$$\text{Grt} + \text{Sil} + \text{Qtz} = \text{Crd} \quad (9)$$

under further decompression, or the reaction

$$\text{Grt} + \text{Kf} + \text{Melt} = \text{Crd} + \text{Bt} \quad (10)$$

under cooling (Spear, Kohn & Cheney, 1999).

The regrowth of Sil between Crd and Spl (Fig. 3d; see also Schenk, 1989, 1990) suggests cooling after the Crd forming stage. This is documented also by the rehydration reactions

$$\text{Grt} + \text{Kfs} + \text{H}_2\text{O} = \text{Bt} + \text{Sil} + \text{Qtz} \quad (11)$$

$$\text{Grt} + \text{Kfs} + \text{H}_2\text{O} = \text{Bt} + \text{Pl} + \text{Qtz} \quad (12)$$

The shallower samples also show exhaustion of primary muscovite and cordierite both within the peripheral parts of the garnet and as 'corona', after garnet, suggesting mica-dehydration melting and decompression. Several observations suggest rehydration effects at lower temperatures (see also Schenk, 1984) such as:

$$\text{Kfs} + \text{Sil} + \text{H}_2\text{O} = \text{Ms} + \text{Qtz} \quad (13)$$

$$\text{Crd} + \text{Sil} + \text{H}_2\text{O} = \text{St} + \text{Qtz} \quad (14)$$

$$\text{Grt} + \text{Sil} + \text{Bt} + \text{H}_2\text{O} = \text{St} + \text{Qtz} + \text{Ms} \quad (15)$$

$$\text{Crd} + \text{H}_2\text{O} = \text{Mg-Chl} + \text{And} + \text{Qtz} \quad (16)$$

$$\text{Crd} + \text{H}_2\text{O} = \text{Mg-Chl} + \text{Ky} + \text{Qtz} \quad (17)$$

The retrograde formation of And + Chl + Qtz after Crd indicates $P < 4$ kbar on cooling. Most rehydration reactions in shallower and deeper samples operated in the subsolidus region. In the uppermost migmatites, where they are widespread, they involved infiltration of aqueous fluids from an external source. The amount of retrograde Ms increases towards the granitoids (Fig. 1) which intrude the migmatites and might have released H_2O during solidification. The K-feldspar involvment in the rehydration reactions producing muscovite accounts for its absence.

6. *P–T* computations

Grt–Pl–Sil–Qtz (GASP: Koziol & Newton, 1988), Grt–Rt–Ilm–Sil–Qtz (GRAIL: Bohlen, Wall & Boettcher, 1983) and Grt–Crd–Sil–Qtz (Perchuck *et al.* 1985) barometers and Grt–Bt (Hodges & Spear, 1982) and Grt–Crd (Bhattacharya, Mazumdar & Sen, 1988) thermometers have been used for the conventional thermobarometry.

The composition of cores of the porphyroblastic Grt or crystals included in Fe–Mg lacking minerals, of compositions of Bt and Pl cores of the matrix or of Bt protected in Pl or in Grt core, and of Pl included in Bt or in Grt, have been used to evaluate P and T close to the peak conditions. To evaluate decompression we have used the compositions of Crd cores and of the Grt outer core, since cordierite started to form later than the core of garnet being included in its peripheral part. GRAIL equilibrium has also been used to calculate P conditions at this stage. To evaluate the late-stage conditions, rim compositions of minerals in textural contact and in separate grains were used. The conventional *P–T* estimates have been calculated at three or four distinct values of T and P; the results are reported in Figure 7. Due to the limited thickness of the studied section, *P–T* conditions reported in Tables 7, 8 and 9 have been

https://doi.org/10.1017/S0016756805001482 Published online by Cambridge University Press

Table 7. Temperatures and pressures estimated for the prograde stage

Sample, spot	*T* (°C)		*P* (kbar)
Deeper samples			
Lfc7			
97Grt-c 105Bt matrix	758	97Grt-c 103Pl-c	6.4
136Grt-c 106Bt matrix	763	136Grt-c 109Pl-c	5.8
Average *PT*	712		6.6
sd	119		1.9
Lfc7a			
141Grt-c 144Bt in Grt	767	141Grt-c 161Pl-c in matrix	7.5
Average *PT*	741		8.2
sd	133		2.2
Sbl88			
77Grt-c in Sil 73Bt in Pl	773	77Grt-c in Sil 121Pl-c in matrix	6.6
Average *PT*	745		7.2
sd	131		2.1
Shallower samples			
Sbl6a			
51Grt-c 53Bt in Pl	702	51Grt-c 155Pl-c	5.9
49Grt-c 95Bt in Pl	669	157Grt-c 155Pl-c	5.1
97Grt-c 53Bt in Pl	692	97Grt-c 104Pl-c in Grt	7.1
97Grt-c 149Bt adjacent	719	97Grt-c 100Pl-c	5.5
97Grt-c 106Bt in Pl	698	204Grt-c 104Pl	7.3
202Grt-c 106Bt in Pl	742	204Grt-c 207Pl	6.1
		204Grt-c 200Pl	6.0
Average *PT*	702		6.3
sd	157		2.4
Sbl54			
127Grt-c 64Bt in matrix	584	127Grt-c 129Pl-c	5.5
127Grt-c 62Bt in matrix	592	131Grt-c 129Pl-c	4.4
Average *PT*	575		4.2
sd	100		1.6
Sbl49			
167Grt-c 169Bt-in matrix	708	167Grt-c 164Pl-c	4.8
85Grt-c 84 Bt in matrix	714	85Grt-c 87Pl-c adjacent Grt	4.5
		170Grt-c 172Pl-c	4.8
Average *PT*	692		4.3
sd	149		2.0

Conventional thermobarometry: Grt–Bt thermometer (Hodges & Spear, 1982) at $P = 7$ kbar and GASP (Koziol & Newton, 1988) at T = 700 °C. Average *PT* using Thermocalc 3.25 program (Powell & Holland, 1994) on a set of three independent reactions. sd – standard deviation.

constrained at *P* of 7 and 5 kbar and at *T* of 700 °C and 600 °C.

Since the shallower and deeper metapelites in the studied profile experienced dehydration melting of micas, *T* estimates around or exceeding 700 °C at $P = 7$ kbar (Table 7) have to be considered as realistic. The Grt–Bt estimates concentrate around the mean values of 705 ± 21 °C and 765 ± 6 °C for the shallower and deeper samples, respectively. These *T* estimates roughly coincide with those derived from the Grt X_{Fe} isopleths calculated by Spear, Kohn & Cheney (1999), using the core compositions. Temperatures of 650–515 °C and 593–475 °C have been calculated on cooling for deeper and shallower samples respectively. The calculated pressures at 700 °C are: (1) for the deeper samples, 5.8 to 7.5 kbar (GASP calibration); 6.2 and 6.4 kbar (Grt–Crd and GRAIL barometers, Table 8); (2) for the shallower samples, 4.4 to 7.3 kbar (GASP, Table 7) and 4.8 kbar (Grt–Crd barometer, Table 8). The pressures calculated at 600 °C are 5.1 to 4.1 kbar and 4.1 to 3.3 kbar for the deeper and shallower samples, respectively, using the rim composition for GASP and Grt–Crd calibrations (Table 9).

It is evident that the GASP equilibrium is strongly temperature-dependent and the estimation of *P* at high *T* also gives different values within the same sample using different pairs. This might reflect the combined effects of the low grossular contents of garnet and of the diachronic mineral re-equilibration. In contrast to GASP equilibrium, the garnet–cordierite–sillimanite–quartz and GRAIL equilibria appear nearly temperature-independent and may be preferred for pressure estimates at the Crd-stability stages. The textural relations involving garnet–cordierite and rutile–ilmenite, as well as the occurrence of relict phengitic white mica (Si/11 ox = 3.26–3.29) in restitic layers, seem to be indicative of a former stage at higher

https://doi.org/10.1017/S0016756805001482 Published online by Cambridge University Press

Table 8. Temperatures and pressures estimated for the decompressional stage

Sample	*T* (°C)		*P* (kbar)
Deeper sample			
Sbl88			
70Grt-outer c 136Crd-c	700	70Grt-outer c 136Crd-c	6.2
		69Grt-c 119Ilm in Grt	6.4
Average *PT*	631		5.1
sd	70		0.6
Shallower sample			
Sbl54			
128Grt-r 63Crd in matrix	675	128Grt-r 63Crd in matrix	4.8
Average *PT*	615		5.5
sd	75		0.8

Conventional thermobarometry: Grt–Crd thermometer (Bhattacharya, Mazumdar & Sen, 1988) at 5 kbar and GRAIL (Bholen, Wall & Boettcher, 1983), Grt–Crd–Sil–Qtz barometry (Perchuck *et al.* 1985) at $T = 700$ °C. Average *PT* using Thermocalc 3.25 program (Powell & Holland, 1994) on a set of five independent reactions. sd – standard deviation.

Table 9. Temperatures and pressures estimated for the cooling stage

Sample	*T* (°C)		*P* (kbar)
Deeper samples			
Lfc7			
98Grt-r 100Crd in matrix	650	98Grt-r 110Pl-r	5.1
		99Grt-r 111Pl-r	4.6
		98Grt-r 118Pl-r	4.9
Average *PT*, 3 reactions (no Bt)	604		5.5
sd	65		0.5
Sbl88			
82Grt-r 80Bt in matrix	515	82Grt-r 137Crd-r	4.1
82Grt-r 137Crd-r	606	71Grt-r 120Pl-r	4.2
		124Grt-r 123Pl-r	4.6
Average *PT*, 5 reactions	519		4.7
sd	72		0.8
Shallower samples			
Sbl6a			
103Grt-r 92Bt-adjacent Pl	501	103Grt-r 105Pl-r	4.1
148Grt-r 149Bt-adjacent Grt	593	52Grt-r 93Pl-r	3.8
152Grt-r 153Bt-adjacent Grt	591		
150Grt-r 151Bt-adjacent Grt	576		
Average *PT*, 3 reactions	550		3.9
sd	116		1.7
Sbl49			
86Grt-r 83Bt in matrix	580	162Grt-r 163Pl-r	3.3
162 Grt-r 168Bt-in matrix	475		
Average *PT*, 3 reactions	553		3.2
sd	114		1.6

Conventional thermobarometry: Grt–Bt and Grt–Crd thermometers (Hodges & Spear, 1982; Bhattacharya, Mazumdar & Sen, 1988) at $P = 5$ kbar and GASP (Koziol & Newton, 1988) at $T = 600$ °C. Average *PT* using Thermocalc 3.25 program (Powell & Holland, 1994) on a set of three or five independent reactions. sd – standard deviation.

pressure. This is in agreement with some higher *P* estimates using GASP equilibrium at high *T* for both the shallower and the deeper samples and with the 'pseudosection' modelled by Tinkham, Zuluaga & Stowell (2001) in the system MnNCKFMASH using an averaged composition of metapelites. The pseudosection predicts, in the range of *T* 650–700 °C and of *P* 7–10 kbar, the assemblage Grt–Bt–Ms–Ky–Pl–Qtz, similar to that supposed for the shallower samples before the partial melting started. *P–T* estimates for shallower and deeper samples were also tested by means of the Thermocalc computer program (version 3.25, Powell & Holland, 1994). Grt–Bt–Pl–Sil–Qtz, Grt–Crd–Bt–Pl–Kfs–Sil–Qtz and Grt–Crd–Pl–Sil–Qtz assemblages have been used to compute prograde, decompressional and cooling conditions. The activities of end members of solution solid phases have been calculated at 7 kbar, 700 °C; 5 kbar, 700 °C; and 5 kbar, 600 °C, relative to prograde, decompressional and cooling stages. The averages of *P–T* are given in

https://doi.org/10.1017/S0016756805001482 Published online by Cambridge University Press

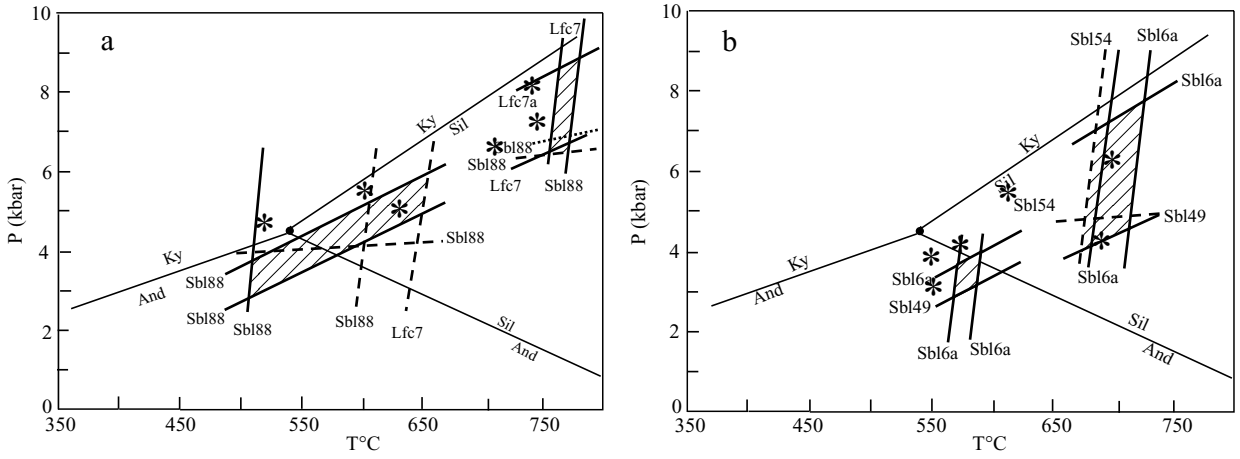

Figure 7. *P–T* estimates by conventional thermobarometry and average *P–T* calculated by Thermocalc computer program for deeper (a) and shallower (b) samples during decompression and cooling. Triple point after Pattison (1992). The Grt–Crd and GRAIL estimates are indicated with dashed and dotted lines, respectively; for the sake of clarity, only the range of *P* and *T* estimates deduced using GASP equilibrium and Grt–Bt pairs have been plotted (thick lines). For the temperature estimates during partial melting, only the realistic values have been considered: (1) *T* around 705 °C and 765 °C during partial melting of the shallower and deeper samples, respectively, consistently with the more limited Bt-dehydration melting of the shallower migmatites (Fornelli *et al.* 2002); (2) *T* estimates of 475 °C and 501 °C on cooling in the shallower samples have been omitted since they intercept GASP estimates at *P* values, precluding the formation of the retrograde kyanite, which on the contrary, is present. Stars indicate average *PT* by Thermocalc.

Tables 7, 8 and 9 and Figure 7. Even if Crd-bearing assemblages are better constrained, all estimates show a high standard of deviation, indicating significant scatter of equilibria.

Thus the computed data must be considered with caution. In any case, by combining these results with the textural data, the composition of the mineral phases and the observed and inferred reactions, some useful information can be derived. Since the shallower samples record a more complete metamorphic history, the relative *P–T* path as been approximated in the NaKFMASH petrogenetic grid (Fig. 8). It shows: (1) a prograde arm composed of an initial part characterized by increase of *P* and *T* within the stability field of kyanite until the *P*-peak, followed by progressive heating up to $T > 700$ °C within the stability field of sillimanite, during which dehydration melting of metapelites occurred, and further followed by isothermal decompression arrested at 3–4 kbar, during which partial melting continued through reaction (5); (2) cooling and rehydration at low pressure.

The lowest temperature reactions observed in the shallower samples produced muscovite with low phengite contents, chlorite, andalusite and kyanite (reactions 15 and 16). From the cordierite-forming stages to the cooling, the *P–T* trajectory depicted by the shallower samples is quite similar to that shown for the upper part of the lower crustal sections of the Serre by Schenk (1984, 1990). The earlier track of the *P–T* path instead appears indicative of a *P* peak, in the stability field of kyanite, pre-dating the *T* peak. From inspection of Figure 7 and Tables 7, 8 and 9, there appears to be a gap of *T* and *P* estimates between the shallower samples (Sbl6a, Sbl49, Sbl54) and sample Sbl88, all coming from a segment only ~ 600 m thick. The uncertainties, however, are relevant and decidedly higher than the calculated differences.

One problem must be addressed at this point. The *P–T* conditions, calculated from thermobarometry and deduced from the relict phases in migmatitic metapelites, should stabilize the Grt + Cpx + Qtz assemblage in Qtz-tholeiitic compositions. This happens if the conditions of Green & Ringwood's (1972) experiments are extrapolated at lower temperature and pressure. In the Serre lower crustal section, such an assemblage has been so far found as 'coronas' around Opx and between Opx and Pl (Paglionico & Piccarreta, 1976; Schenk, 1984) and has been interpreted as reflecting cooling (Schenk, 1984).

7. Tectonic implications

The pre-migmatization stage under increasing *P* and *T* originated within a tectonic setting of crustal thickening in agreement with pre-granite emplacement nappe piling. In fact, the tectonic units of the upper part of the crustal section of the Serre indicate thermal metamorphic overprint (Colonna, Lorenzoni & Zanettin Lorenzoni, 1973). Migmatization took place upon deformation (Schenk, 1984; Del Moro, Fornelli & Piccarreta, 2000*a*; Fornelli *et al.* 2002) and extraction of granitic melts occurred mainly during the decompression (Fornelli *et al.* 2002). Decompression from Grt production to Crd formation around Grt and cooling from sillimanite to andalusite and kyanite stability fields suggest a *P–T* path where decompression

https://doi.org/10.1017/S0016756805001482 Published online by Cambridge University Press

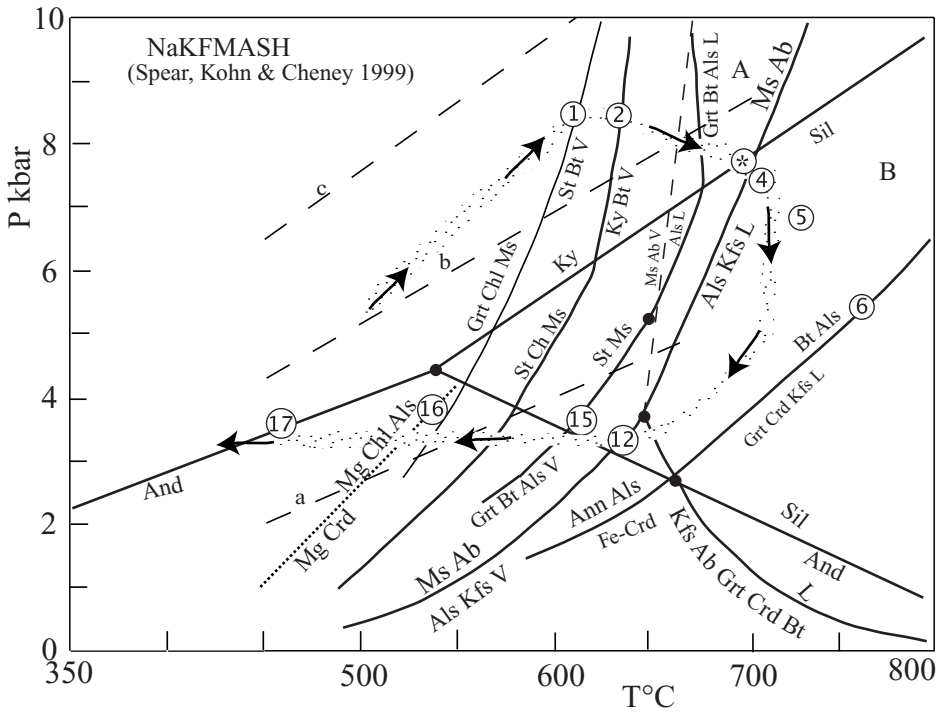

Figure 8. *P–T* trajectory shown by the shallower samples. The figures indicate the reactions described in the text. 'A' is melting region from vapour-saturated (asterisk) to vapour-absent conditions predicted for the pelitic system; experimental studies have shown that in this region, sodic melts (like most of the leucosomes of the studied profile) and peritectic staurolite (part of the relict St_1?) form at *T* around 700 °C under *P* of 6–10 kbar (Patiño Douce & Harris, 1998; Garcìa Casco *et al.* 2003). 'B' is region characterized by melting reactions Bt + Sil + Qtz + Pl = Grt + Kfs + L or Mg–Crd + Kfs + L, depending on the Mg of the bulk composition; 'a' Ms with $Si_{11ox} = 3.10$; 'b' Ms with $Si_{11ox} = 3.20$; 'c' Ms with $Si_{11ox} = 3.30$ (Massone *in* Brouwer, Vissers & Lamp, 2002). Triple point after Pattison (1992). Reaction curves in the NaKFMASH system after Spear, Kohn & Cheney (1999). Reaction MgCrd = MgChl + Als in KMASH system.

dominated at high temperature, while cooling was progressively more important at low pressure.

This type of path indicates either rapid erosion or tectonic extension. It seems that this part of the Serre section suffered some ablation, because: (1) decompression and non-pervasive high-*T* mylonitic deformation, accompanied by boudinage and elongation of minerals and formation of pull-apart filled with low-pressure minerals, are correlated, and (2) the Cardinale tonalites (Fig. 1) were consolidated under *P* of about 5.5 kbar (Caggianelli, Prosser & Del Moro, 2000), whereas the migmatites which they intruded record higher fossil pressures and were intruded by anatectic melts when they were not completely consolidated (A. Caggianelli, unpub. Ph.D. thesis, Bari Univ. 1988).

On the other hand, isothermal decompression and subsequent isobaric cooling are characteristics of a path produced by tectonic denudation (e.g. Ruppel & Hodges, 1994). The tectonic denudation of the Serre granulite terrane might have been caused by a major extensional shear zone along which the granitoids were emplaced (Del Moro, Fornelli & Piccarreta, 2000*b*; Caggianelli & Prosser, 2002). The mass balance between the removed overburden and the emplaced plutonics should have been responsible for the decompression (see also Caggianelli & Prosser, 2002). Since the granitoids form a ~10 km thick 'layer', about 20 km of rocks should have been removed before or during the emplacement of the granitoids. This explains the discrepancy between the *P* estimated within the tonalites and the fossil *P* values recorded within the migmatites that they intruded.

Thermal equilibration after crustal thickening and processes operating at the crust–mantle boundary, producing huge volumes of magmas which migrated upward forming the plutonic 'layer' in an extensional regime, might have been responsible for progressive heating after the *P* peak shown by migmatites. The important subsolidus rehydration in the vicinity of the granitoids implies reactions with H_2O released by consolidating plutonics. Reset Bt-ages coincident with ages of extensional phases in circum-mediterranean areas in the Mesozoic times (Del Moro, Fornelli & Piccarreta, 2000*b*) and pull-aparts filled by low-grade minerals (Fig. 2c) indicate that extensional tectonics also operated during post-Hercynian times (Del Moro, Fornelli & Piccarreta, 2000*b*; Caggianelli, Prosser & Del Moro, 2000; Caggianelli & Prosser, 2002).

This interpretation differs from that proposed for Calabria by Schenk (1990) and Graessner & Schenk (1999), who frame the crustal thickening, the granitoid

https://doi.org/10.1017/S0016756805001482 Published online by Cambridge University Press

intrusions and the subsequent isothermal decompression in a contractional context.

8. Conclusions

On the basis of textural features, relict phases and mineral reactions, as well as thermobarometric computations, the *P–T* path of the uppermost part of the migmatite–granulite terrane of the Serre has been proposed from prograde to retrograde stages.

This path is interpreted as reflecting crustal thickening and subsequent thinning stages. Thermal equilibration and the processes operating at the crust–mantle boundary (producing huge volumes of 'granitic' melts, which migrated upward) cooperated for progressive heating from the end of the contractional stage to the occurrence of a major tectonic denudation, which caused a dramatic period of decompression. An extensional regime was also active during post-Hercynian times. Partial melting was initiated along the prograde trajectory in the presence of free water, producing most of the '*in situ*' leucosomes, and continued during decompression through the dehydration melting of micas producing leucogranitic melts which mostly migrated far from the source and mixed with or intruded the granitoids at various structural levels (Fornelli *et al.* 2002).

Acknowledgements. V. Schenk is thanked for his criticism on a previous version of the paper. The careful reviews by P. Barbey and A. Garcia Casco of the present version significantly improved the manuscript. J. Holland is also thanked for suggestions and editorial assistance. Financial support by MIUR (cofin 2001) and Bari University.

References

Amodio Morelli, L., Bonardi, G., Colonna, V., Dietrich, D., Giunta, G., Ippolito, F., Liguori, V., Lorenzoni, S., Paglionico, A., Perrone, V., Piccarreta, G., Russo, M., Scandone, P., Zanettin Lorenzoni, E. & Zuppetta, A. 1976. L'arco calabro-peloritano nell' orogene Appenninico-Maghrebide. *Memorie Società Geologica Italiana* **17**, 1–60.

Ayuso, R. A., Messina, A., De Vivo, B., Russo, S., Woodruff, L. G., Sutter, S. F. & Belkin, H. E. 1994. Geochemistry and argon thermochronology of the Variscan Sila batholith, southern Italy: source rocks and magma evolution. *Contributions to Mineralogy and Petrology* **117**, 87–109.

Bhattacharya, A., Mazumdar, A. C. & Sen, S. K. 1988. Fe–Mg mixing in cordierite: constraints from natural data and implications for cordierite–garnet thermometry in granulites. *American Mineralogist* **3**, 338–44.

Bohlen, S. R., Wall, V. J. & Boettcher, A. L. 1983. Experimental investigations and geological applications in the system FeO–TiO_2–Al_2O_3–SiO_2–H_2O. *American Mineralogist* **68**, 1049–58.

Bonardi, G., Cavazza, W., Perrone, V. & Rossi, S. 2001. Calabria-Peloritani terrane and northern Ionian Sea. In *Anatomy of an Orogen: the Apennines and Adjacent Mediterranean Basins* (eds G. B. Vai and I. P. Martini), pp. 287–306. Kluwer Academic Publishers (Great Britain).

Bonardi, G., Cello, G., Perrone, V., Tortorici, L., Turco, E. & Zuppetta, A. 1982. The evolution of the northern sector of the Calabria-Peloritani-Arc. In a semiquantitative palynspastic restoration. *Bollettino della Società Geologica Italiana* **101**, 259–74.

Borghi, A., Colonna, V. & Compagnoni, R. 1992. Structural and metamorphic evolution of the Bocchigliero and the Mandatoriccio complexes in the Sila nappe (Calabrian-Peloritan Arc, Southern Italy). In *Contributions to the Geology of Italy with Special Regards to the Paleozoic Basement* (eds L. Carmignani and F. P. Sassi), pp. 321–34. IGCP no. 276, Newsletter 5, Siena.

Brouwer, F. M., Vissers, R. L. M. & Lamp, W. M. 2002. Structure and metamorphism of the Gran Paradiso massif, western Alps, Italy. *Contributions to Mineralogy and Petrology* **143**, 450–70.

Brown, M. 1993. *P–T–t* paths of orogenic belts and the causes of regional metamorphism. *Journal of Geological Society, London* **150**, 227–31.

Caggianelli, A., Del Moro, A., Paglionico, A., Piccarreta, G., Pinarelli, L. & Rottura, A. 1991. Lower crustal granite genesis connected with chemical fractionation in the continental crust of Calabria (Southern Italy). *European Journal of Mineralogy* **3**, 159–80.

Caggianelli, A. & Prosser, G. 2002. Modelling the thermal perturbation of the continental crust after intraplating of thick granitoid sheets: a comparison with the crustal sections in Calabria (Italy). *Geological Magazine* **139**, 699–706.

Caggianelli, A., Prosser, G. & Del Moro, A. 2000. Cooling and exhumation history of deep-seated and shallow level, late hercynian granitoids from Calabria. *Geological Journal* **35**, 33–42.

Colonna, V., Lorenzoni, S. & Zanettin Lorenzoni, E. 1973. Sull'esistenza di due complessi metamorfici lungo il bordo sud-orientale del massiccio "granitico" delle Serre (Calabria). *Bollettino della Società Geologica Italiana* **92**, 801–30.

Colonna, V. & Piccarreta, G. 1975. Schema strutturale della Sila Piccola meridionale. *Bollettino della Società Geologica Italiana* **94**, 3–16.

Del Moro, A., Fornelli, A. & Piccarreta, G. 2000*a*. Disequilibrium melting in granulite facies metasedimentary source of the northern Serre (Calabria – Southern Italy). *Mineralogy and Petrology* **70**, 89–104.

Del Moro, A., Fornelli, A. & Piccarreta, G. 2000*b*. Tectonothermal evolution of the hercynian continental crust of the Serre (Southern Calabria – Italy) monitored by Rb–Sr biotite resetting. *Terra Nova* **12**, 239–44.

Dietrich, D. 1988. Sense of overthrust shear in the Alpine nappes of Calabria (southern Italy). *Journal of Structural Geology* **10**, 373–81.

Fornelli, A., Piccarreta, G., Acquafredda, P., Micheletti, F. & Paglionico, A. 2004. Geochemical fractionation in migmatitic rocks from Serre granulitic terrane (Calabria, southern Italy). *Periodico di Mineralogia* **LXXIII**, Special Issue n. 2, 145–57.

Fornelli, A., Piccarreta, G., Del Moro, A. & Acquafredda, P. 2002. Multistage-melting in the lower crust of the Serre (southern Italy). *Journal of Petrology* **43**, 2191–217.

GARCÌA CASCO, A., HAISSEN, F., CASTRO, A., EL-HMIDI, H., TORRES-ROLDÀN, R. L. & MILLÀN, G. 2003. Synthesis of Staurolite in Melting Experiments of a Natural Metapelite: Consequences for the Phase Relations in Low-Temperature Pelitic Migmatites. *Journal of Petrology* **44**, 1727–57.

GRAESSNER, T. & SCHENK, V. 1999. Low pressure metamorphism of Paleozoic pelites in the Aspromonte, southern Calabria: constraints on the thermal evolution in the Calabrian crustal cross-sections during the Hercynian orogeny. *Journal of Metamorphic Geology* **17**, 157–72.

GRAESSNER, T. & SCHENK, V. 2001. An exposed Hercynian deep crustal section in the Sila Massif of Northern Calabria: mineral chemistry, petrology and a P–T path of granulite-facies metapelitic migmatites and metabasites. *Journal of Petrology* **42**, 931–61.

GREEN, D. H. & RINGWOOD, A. E. 1972. A comparison of recent experimental data on the gabbro-eclogite transition. *Journal of Geology* **80**, 277–88.

HODGES, K. V. & SPEAR, F. S. 1982. Geothermometry, geobarometry and the Al_2SiO_5 triple point at Mt. Moosilauke, New Hampshire. *American Mineralogist* **67**, 1118–34.

KOZIOL, A. M. & NEWTON, R. C. 1988. Redetermination of the anorthite breakdown reaction and improvement of the plagioclase–garnet–Al_2SiO_5–quartz barometer. *American Mineralogist* **73**, 216–23.

KRETZ, R. 1983. Symbols for rock-forming minerals. *American Mineralogist* **34**, 345–68.

KRUHL, J. H. & HUNTEMANN, T. 1991. The structural state of the former lower continental crust in Calabria (S. Italy). *Geologische Rundschau* **80**, 289–302.

LORENZONI, S. & ZANETTIN LORENZONI, E. 1983. Note illustrative della carta geologica della Sila. *Memorie della Società Geologica Università di Padova* **36**, 317–42.

MASSONNE, H. & SCHREYER, W. 1987. Phengite geobarometry based on the limiting assemblage with K-feldspar, phlogopite and quartz. *Contributions to Mineralogy and Petrology* **96**, 212–24.

PAGLIONICO, A. & PICCARRETA, G. 1976. Le Unità del Fiume Pomo e di Castagna nelle Serre settentrionali (Calabria). *Bollettino Società Geologica Italiana* **95**, 1–11.

PAGLIONICO, A. & PICCARRETA, G. 1978. History and petrology of a fragment of the deep crust in the Serre (Calabria, Italy). *Neues Jahrbuch für Mineralogie und Petrographie Mitteilungen, Monatshefte* **9**, 385–96.

PATIÑO DOUCE, A. E. & HARRIS, N. 1998. Experimental constraints on Himalayan anatexis. *Journal of Petrology* **39**, 689–710.

PATTISON, D. R. M. 1992. Stability of andalusite and sillimanite and the Al_2SiO_5 triple point: constraints from the Ballachulish aureole, Scotland. *Journal of Geology* **100**, 423–46.

PERCHUCK, L. L., ARANOVICH, L. Y., PODLESSKII, K. K., LAVRANT'EVA, I. V., GERASIMOV, V. Y., FED'KIN, V. V., KITSUL, V. I., KARASAKOV, L. P. & BERDNIKOV, N. V. 1985. Precambrian granulites of the Aldan shield, eastern Siberia, USSR. *Journal of Metamorphic Geology* **3**, 265–310.

PILUSO, E. & MORTEN, L. 2004. Hercynian high temperature granulites and migmatites from the Catena Costiera, norther Calabria, southern Italy. *Periodico di Mineralogia Special Issue* **LXXII** (2), 159–72.

POWELL, R. & HOLLAND, T. J. B. 1994. Optimal geothermometry and geobarometry. *American Mineralogist* **79**, 120–33.

RECHE, J. & MARTINEZ, F. J. 1996. GPT: An Excel spreadsheet for thermobarometric calculations in metapelitic rocks. *Computers & Geosciences* **22**(7), 775–84.

ROBINSON, P. R., HOLLOCHER, K. T., TRACY, R. J. & DIESCH, C. W. 1982. High grade Acadian regional metamorphism in south-central Massachusetts. *In NEIGC 74th Annual Meeting of the State Geological and natural History Survey of Connecticut, Guidebook for fieldtrips in Connecticut and south-central Massachusetts* (ed. R. Q. S. Joesten), pp. 289–340. Storrs: University of Connecticut.

RUPPEL, C. & HODGES, V. 1994. Pressure–temperature–time paths from two-dimensional thermal models: prograde, retrograde, and inverted metamorphism. *Tectonics* **13**, 17–44.

SCHENK, V. 1980. U–Pb and Rb–Sr radiometric dates and their correlation with metamorphic events in the granulite-facies basement of the Serre, Southern Calabria (Italy). *Contributions to Mineralogy and Petrology* **73**, 23–38.

SCHENK, V. 1984. Petrology of felsic granulites, metapelites, metabasics, ultramafics, and metacarbonates from Southern Calabria (Italy): Prograde metamorphism, uplift and cooling of a former Lower Crust. *Journal of Petrology* **25**, 255–98.

SCHENK, V. 1989. *P–T–t* path of the lower crust in the Hercynian fold belt of southern Calabria. In *Evolution of Metamorphic Belts* (eds J. S. Daly, R. A. Cliff and B. W. D. Yardley), pp. 337–42. Geological Society of London, Special Publication no. 43.

SCHENK, V. 1990. The exposed crustal cross section of southern Calabria, Italy: structure and evolution of a segment of hercynian crust. In *Exposed Cross-Sections of the Continental Crust* (eds M. H. Salisbury and D. M. Fountain), pp. 21–42. Kluwer Academic Publishers.

SPEAR, F. S., KOHN, M. J. & CHENEY, J. T. 1999. P–T paths from anatectic pelites. *Contributions to Mineralogy and Petrology* **117**, 375–93.

THOMPSON, A. B. & CONNOLLY, J. A. D. 1995. Melting of the continental crust: some thermal and petrological constraints on anatexis in continental collision zones and other tectonic settings. *Journal of Geophysical Research* **100**, 15565–79.

TINKHAM, D. K., ZULUAGA, C. A. & STOWELL, H. H. 2001. Metapelite phase equilibria modelling in Mn NCKFMASH: The effect of variable Al_2O_3 and MgO/(MgO+FeO) on mineral stability. *Geological Materials Research* **3**(1), 1–42.

https://doi.org/10.1017/S0016756805001482 Published online by Cambridge University Press